Numerical Simulation of the Aeroacoustic Performance of the DSA380 High-Speed Pantograph Under the Influence of a Crosswind

Yadong Zhang[1, *] and Jiye Zhang[2]

Abstract: The object of research of this paper is the DSA380 high-speed pantograph. The near-field unsteady flow around the pantograph was investigated using large eddy simulation (LES) while the far-field aerodynamic noise was analysed in the frame of the Ffowcs Williams-Hawkings (FW-H) acoustic analogy. According to the results, the contact strip, base frame and knuckle are the main aerodynamic noise sources, with vortex shedding, flow separation and recombination around the pantograph being related key physical factors. The aerodynamic noise radiates outwards in the form of spherical waves when the distance of the noise receiving point is farther than 8 m. The sound pressure level (SPL) grows approximately as the 6th power of pantograph operating speed. The aerodynamic noise energy is mainly concentrated in the region of 400-1000 Hz, and the frequency band is wider with crosswind than without crosswind. The peak frequency displays a linear relationships with the operating speed and crosswind velocity, respectively. The aerodynamic and aeroacoustic generation from the knuckle-downstream orientation of the pantograph is superior to those of the knuckle-upstream orientation model. This finding may be used for the optimal design of future pantograph configurations in the presence of crosswind.

Keywords: Pantograph, crosswind, aeroacoustic performance, large eddy simulation, FW-H acoustic analogy.

1 Introduction

The pantograph is an important current collection device system between the catenary and the pantograph cavity on the top of high-speed trains. However, the complex components of the pantograph greatly influence the aeroacoustic performance of high-speed trains. When a train is running at a high speed, the concave and convex parts on the surface of the pantograph cause severe turbulent disturbance to the airflow, and this turbulence brings about airflow separation and vortex shedding and breaking, thereby generating a strong fluctuation pressure field that converts into aerodynamic noise around the pantograph [Thompson, Latorre Iglesias, Liu et al. (2015); Mellet, Létourneaux,

---

[1] Department of Mechanics and Aerospace Engineering, Southern University of Science and Technology, Shenzhen, 518055, China.

[2] State Key Laboratory of Traction Power, Southwest Jiaotong University, Chengdu, 610031, China.

[*] Corresponding Author: Yadong Zhang. Email: zhangyd3@sustech.edu.cn.

Poisson et al. (2006); Zhang, Zhang and Li (2016)]. An experiment on an eight-coach full-scale passenger train at 350 km/h indicated that the pantograph accounted for approximately 10% of the total aerodynamic noise energy [Zhang, Xiao, Wang et al. (2018)], and that the pantograph system is a major contributor of radiated noise to the interior of the train. To minimize the effect of the pantograph on the interior and exterior noise and allow increases in the operating speed of high-speed trains, it is essential to investigate the aeroacoustic performance of the pantograph.

Current research on the aerodynamic noise of the pantograph mainly focuses on the location and classification of noise sources [Thompson, Latorre Iglesias, Liu et al. (2015); Mellet, Létourneaux, Poisson et al. (2006); Nagakura (2006)], low-noise design based on the main aerodynamic noise sources of the components [Ikeda, Suzuki and Yoshida (2006); Sueki, Ikeda and Takaishi (2009)], and the semi-empirical models that are currently also used in the industry to predict aerodynamic noise from pantographs [Latorre Iglesias, Thompson and Smith (2017)]. However, scholars have analysed the aerodynamic noise characteristics of the pantograph without crosswind conditions [Liu, Hu, Thompson et al. (2018); Yu, Li and Zhang (2013); Zhang, Zhang, Li et al. (2016); Tan, Yang, Tan et al. (2018); Zhang, Zhang, Li et al. (2017); Zhang, Zhang, Zhang et al. (2017)]. Quantitative studies of the aerodynamic noise behaviours and aeroacoustic characteristics of the pantograph under crosswind are rare. Studies have typically focused on the characteristics of aerodynamic loads and corresponding safety issues [Baker (2010)], with less attention to flow-induced noise characteristics. The aerodynamic loads of the pantograph deteriorate rapidly under crosswind conditions [Flynn, Hemida and Baker (2016); Li, Qin and Zhang (2019)]. And the aerodynamic behaviour caused by crosswind also influences the aerodynamic noise of the pantograph. To evaluate the ride comfort of railway vehicles and the environmental influence by aerodynamic noise running under a strong crosswind, it is necessary to estimate the flow-induced noise on pantographs which are caused by the crosswind, as well as understand the aerodynamic behaviour around the pantographs.

In this paper, more details of flow behaviour, aeroacoustic behaviour and the corresponding aerodynamic noise mechanisms of a full-scale pantograph for both knuckle-downstream and knuckle-upstream operation models are investigated under crosswind. Finally, we quantitatively analyse the aerodynamic noise with respect to several crosswind velocity levels, acoustic attenuation with respect to transverse distance, frequency spectral distribution regularity, the aerodynamic noise contribution of both the whole pantograph and its components.

The paper is structured as follows: Section 2 presents the large eddy simulation (LES) turbulent model, the Ffowcs Williams-Hawkings (FW-H) acoustic analogy applied in this research. Section 3 introduces the numerical computational model, the computational domain, the boundary condition. Additionally, grid-independent validation is verified in this paper. In Section 4, the instantaneous vorticity and vortex structure formation based on the Q-criterion around the pantograph are presented and investigated. The far-field aerodynamic noise characteristics are presented and analyzed in Section 5. Finally, the conclusions and an outlook are given in Section 6.

2 Computational approaches

Computational fluid dynamics (CFD) are used to simulate the air flow around the pantograph, and computational aeroacoustics (CAA) are used to calculate the aerodynamic noise [Thompson, Latorre Iglesias, Liu et al. (2015); Zhang, Zhang, Li et al. (2017)].

2.1 LES model

Complicated vortexes shed and recombine in the wake region of the pantograph and its components. These vortex structures are dominated by large turbulent structures. Most of these large vortex structures can be resolved directly using the LES turbulence model, and only the influence of small-scales vortex structures on large-scale vortexes that are smaller than computational cells is modelled using the LES filter function [Sagaut (2006)]. The LES model has a strong ability to obtain the detailed transient flow field information required for the numerical simulation of aerodynamic noise. In addition, the dynamic fluid flow characteristics can be captured using the LES turbulence model. Therefore, the LES model is applied to predict the flow-induced aerodynamic behaviour of the pantograph under crosswind.

2.2 FW-H acoustic analogy

In this paper, the FW-H acoustic analogy approach is adopted to calculate radiated noise generated by the pantograph in the external sound field under crosswind.

The Lighthill sound analogy theory was first derived by Lighthill [Lighthill (1952)] and is widely used to solve aircraft injection noise. Then, to reduce the influence of the solid wall on aeroacoustics, aeroacoustic theory was further extended by Curle [Curle (1955)]. Subsequently, to reduce the influence of the moving object boundary on the aeroacoustic problem, in 1969, Ffowcs-Williams et al. [Ffowcs-Williams and Hawkings (1969)] developed the FW-H acoustic analogy by using the generalized function method. This differential FW-H equation (Eq. (1)) may be written as:

$$\left(\frac{1}{c_0^2} \frac{\partial^2}{\partial t^2} - \frac{\partial^2}{\partial x_i^2} \right) \left[H(f) p' \right] = \frac{\partial}{\partial t} \left\{ \left[\rho(u_n - v_n) + \rho_0 v_n \right] \delta(f) \right\}$$

$$- \frac{\partial}{\partial x_i} \left\{ \left[\rho u_i (u_n - v_n) + p_{ij} n_j \right] \delta(f) \right\} + \frac{\partial^2}{\partial x_i \partial x_j} \left[T_{ij} H(f) \right] \tag{1}$$

$$T_{ij} = \rho u_i u_j + \left[(p - p_0) - c_0^2 (\rho - \rho_0) \right] \delta_{ij} - \tau_{ij} \tag{2}$$

$$p_{ij} = (p - p_0) \delta_{ij} - \tau_{ij} \tag{3}$$

where p' is the sound pressure, $p' = p - p_0$, p_0 is the initial air pressure, p is the static air pressure, c_0 is the speed of sound, ρ is the static air density, ρ_0 is the initial air density, u_n is the normal velocity in the flow medium, v_n is the normal surface velocity in the moving solid medium, u_i is the flow velocity in the i direction, u_j is the flow velocity in the j direction, p_{ij} is the stress tensor, n_j is the component of the unit external

normal vector on the surface of the object in the x_j direction, T_{ij} is the Lighthill stress tensor, $\delta(f)$ is the Dirac delta function, and $H(f)$ is Heaviside function.

The first, second and third terms on the right side of Eq. (1) represent the monopole sources, dipole sources and quadrupole sources, respectively. Because low Mach number flow is simulated for the pantograph under crosswind, the quadrupole sources from the Lighthill stress tensor may be neglected [Zhang, Zhang and Li (2016); Yu, Li and Zhang (2013)]. Also, the monopole sources do not need to be considered because the pantograph surface can be seen as arbitrary rigid bodies and without moving in the fluid field, and the pulsating volume quantity becomes zero [Zhang, Zhang and Li (2016)], that is $v_n = 0$.

The far-field aerodynamic noise in the pantograph can be obtained based on the fluctuating pressure on the surface of the pantograph.

3 Computational model

3.1 DSA380 high-speed pantograph model

The physical model is a geometric structure of the DSA380 pantograph system used on CRH380B high-speed trains in China. In this paper, we divide the DSA380 pantograph into 10 components and then classify these components into four areas, namely, the panhead, framework, base frame and insulators. The panhead consists of the contact strip, balance arm, and panhead support. The framework includes the balance rod, upper arm rod, pull rod, lower arm rod and knuckle. The geometric structure of the DSA380 high-speed pantograph is shown in Fig. 1.
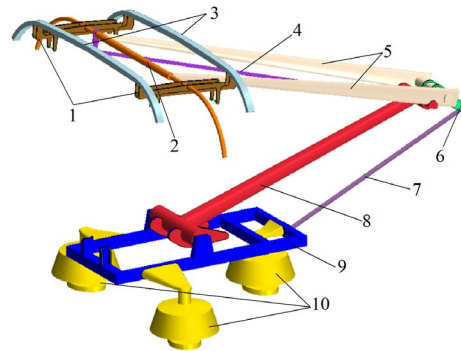

Figure 1: The DSA380 high-speed pantograph. The list of components in the figure is as follow. 1: panhead support; 2: balance arm; 3: contact strip; 4: balance rod; 5: upper arm rod; 6: knuckle; 7: pull rod; 8: lower arm rod; 9: base frame; 10: insulators

3.2 Computational domain and boundary conditions

An analogue wind tunnel model is used to construct a computational domain for the pantograph under crosswind, as shown in Fig. 2. The computational domain is 30 $L \times$6 $H \times$15 W. And the pantograph overall dimensions are L=2.436 m, H=1.633 m, and W=2.024 m along the x, y, and z directions, respectively.

The front side of the computation domain is set as the velocity inlet boundary condition, which the velocity magnitude is the pantograph operating speed. The left side is also set as the velocity inlet boundary condition, and the velocity amplitude is the crosswind velocity. The rear side and right side are defined as the pressure outlet boundary conditions, which is 0 Pa and 101,325 Pa for the gauge pressure and reference pressure, respectively. The top side is defined as symmetrical with respect to the boundary. The surface of the pantograph is set as a no-slip wall boundary condition. To achieve an analogue ground effect, the ground can be set as a slipping surface in the boundary conditions.

The pantograph is situated in the knuckle-downstream orientation model when the airflow direction goes from the front side to the rear side, as shown in Fig. 2, while the pantograph is situated in the knuckle-upstream orientation model when the airflow direction goes from the rear side to the front side, as shown in Fig. 2.
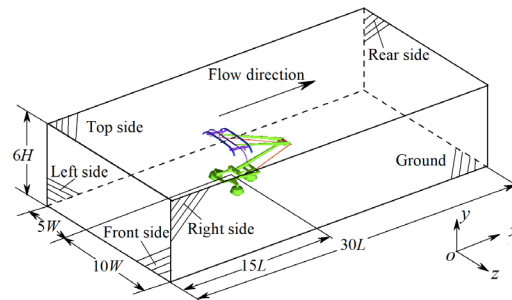

Figure 2: Computation domain

In this paper, the software package STAR-CCM+10.06 is used to perform flow field simulation and aeroacoustic computation. The K-Epsilon turbulence is selected to provide an initial steady value to solve the unsteady LES turbulence simulation. After the flow field is fully developed and the surface fluctuating pressure of the panhead has a certain periodicity, the transient flow field data is stored in the intermediate file for the FW-H integral equation of the sound field calculation. In this simulation, we choice the time step and physical time of the aerodynamic noise calculation is 1×10^{-4} s and 0.5 s, which ensure the maximum frequency and frequency resolution is 5000 Hz and 2 Hz, respectively.

3.3 Grid-independent validation

Five sets of grids are configured for grid-independent validation, for which Surface Remesher and Trimmer are used to generate spatial discrete grids. The grid configurations and computational results are compared in Tab. 1. To reduce the influence of the pantograph wall surface and the wake region on air flow, the spatial grid is discretized by combining the boundary layer grid on the pantograph surface and the local grid encryption technology during the discrete grid process. Four block areas are encrypted in the wake region of the pantograph in the longitudinal direction and the transverse direction is shown in Fig. 3. The SPL of Grid-1 is 1.1 dBA higher than that of Grid-2 and 0.7 dBA higher than that of Grid-3. However, as the grids are further refined,

the SPLs of Grid-4 and Grid-5 show little change. Therefore, Grid-3 meets the requirement of grid independence.

Table 1: Grid configurations and computational results.

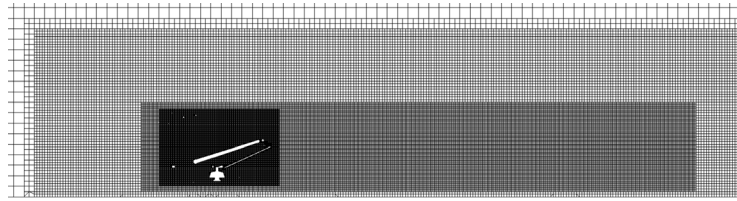| Grids	Grid number (millions)	First layer thickness (mm)	Boundary layer number	Stretching ratio	Surface minimum grid (mm)	Surface maximum grid (mm)	SPL (dBA)
Grid-1	55.03	0.1	8	1.1	1	15	105.4
Grid-2	59.66	0.1	8	1.1	0.5	10	104.3
Grid-3	66.41	0.1	10	1.1	0.5	8	104.7
Grid-4	71.32	0.1	12	1.1	0.3	8	104.6
Grid-5	73.59	0.1	16	1.1	0.2	6	104.9

Figure 3: Computational grids

In addition, the resultant velocity amplitudes of the panhead obtained from the three grids are compared in Fig. 4. As the distance from the panhead increases, the velocity amplitude distribution curves first increase rapidly, then decrease and increase on the panhead region, and finally decrease gradually again. When the longitudinal distance is 3.05 m, the velocity amplitude reaches a maximum. The comparison of different grid scales shows that the three sets of grid distribution regions and the velocity magnitude have good consistency with little difference. It can be seen that the Grid-3 grid strategy can meet grid independence requirements.
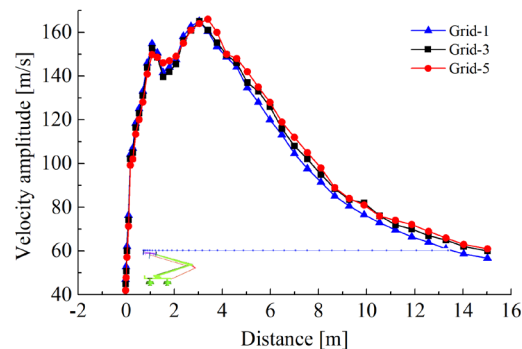

Figure 4: Comparison for the velocity amplitudes between the three grids

4 Flow behaviour around the pantograph

To identify the effects of operation orientation and the development process of the vortex shedding on the flow behaviour around the pantograph under crosswind, instantaneous vorticity magnitude and vortex structures are each discussed. If not mentioned below in this research, the pantograph operating speed is also 350 km/h, and the crosswind velocity is still 15 m/s.

The transient vorticity magnitude in the longitudinal symmetry plane is represented in Fig. 5, which illustrates the distribution of strong and weak eddies. Vorticity is measured in units of s^{-1}. There are three-dimensional vortexes with different rotational directions and different scales in the windward position of the panhead, knuckle, base frame and insulators. Simultaneously, for the formation of the vortex at the position of the pantograph, the vortex keeps falling off and recombining in the waking of the pantograph, and the large vortex keeps breaking and forming small vortexes. These vortexes are finally affected by the fluctuating pressure of the pantograph and form an aerodynamic noise source. Compared with the knuckle, the larger vortex takes place in the region of the panhead, base frame and insulators. Thus, vortex shedding, flow separation and recombination are the main controlling factors of aerodynamic noise generated by the pantograph.

Compared with the substantial vorticity distribution of the pantograph with different knuckle-downstream and knuckle-upstream orientation models, the higher vorticity distribution range of the pantograph running in knuckle-upstream orientation model is wider than that running in knuckle-downstream orientation model. Additionally, due to the Kármán vortex street phenomenon, the aerodynamic noise spectrum of the pantograph includes the peak frequencies related to the key components of the panhead.
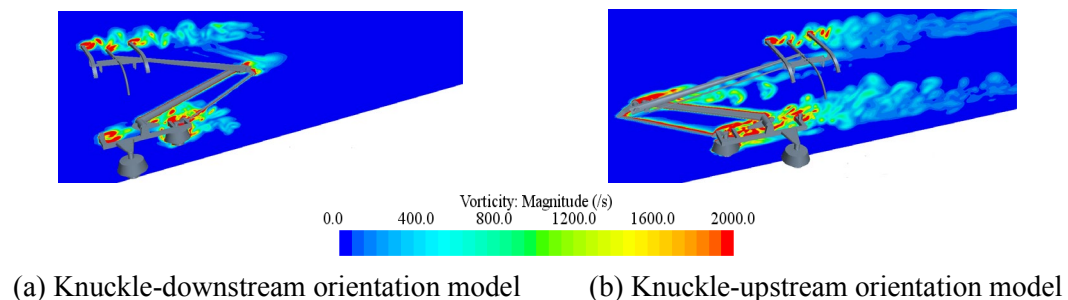

Vorticity: Magnitude (/s)
0.0   400.0   800.0   1200.0   1600.0   2000.0

(a) Knuckle-downstream orientation model   (b) Knuckle-upstream orientation model

Figure 5: Instantaneous vorticity magnitude in the longitudinal symmetry plane

The formation process of vortex fragments is precisely captured from time t=0.3 s to 0.4 s with a Q-value of 10,000. The formation process of the crescent-shaped eddies is marked by the elliptical shape. Small belt-shaped eddies shed from the contact strip move downward to converge with the knuckle area and the base frame area of the eddies to form large crescent-shaped eddies. These eddies subsequently breakdown into small-scale eddies, which continue to transform into line-shaped eddies with large-scale shapes. This cycle continues and the results show that the eddies from the pantograph reattach, shed, separate and recombine in a periodic cycle, as illustrated globally in Fig. 6.
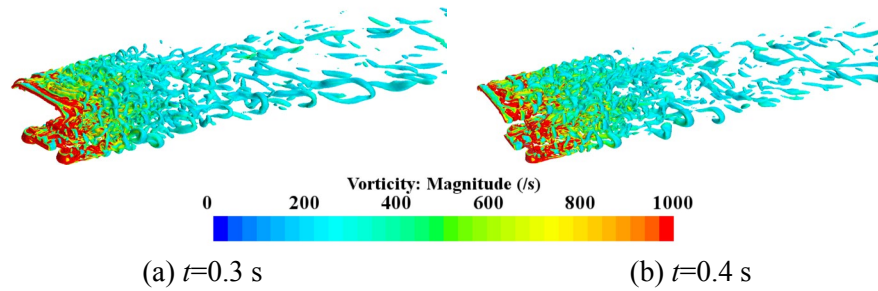
(a) *t*=0.3 s   (b) *t*=0.4 s

Figure 6: Formation process of vortexes based on the Q-criterion, coloured by vorticity magnitude

To illustrate the effects of the pantograph's operating orientations on flow behaviours, the transient vorticity distribution based on the Q-criterion and coloured by the velocity magnitude is shown in Fig. 7 with a Q-value of 10,000. There are small vortexes on the windward side of the pantograph but larger vortexes on the leeward side of the pantograph under crosswind. Additionally, vortex shedding and recombination have a more negative influence on the flow field in the knuckle-upstream orientation model than in the knuckle-downstream orientation model.

In conclusion, the comparison of transient vortexes and vortex structures for different pantograph operating orientations reveals that the flow behaviour characteristics and aerodynamic performance of the knuckle-downstream orientation model are superior to those of the knuckle-upstream orientation model under crosswind.
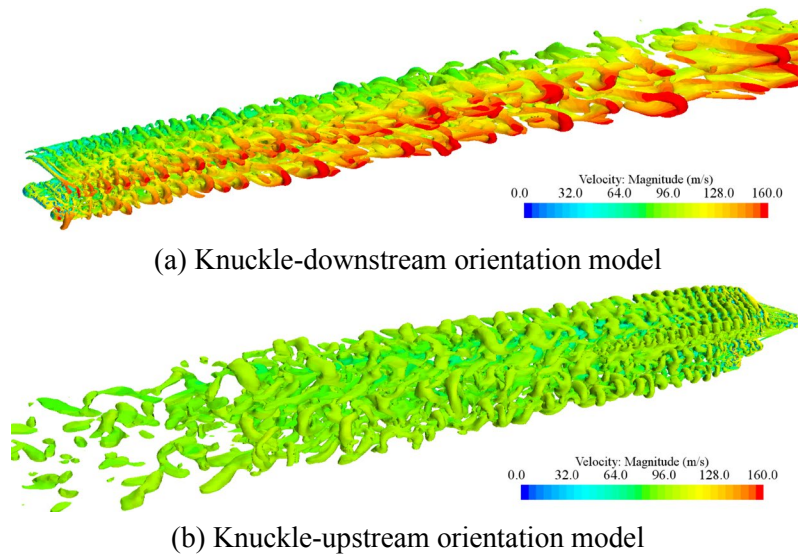

(a) Knuckle-downstream orientation model

(b) Knuckle-upstream orientation model

Figure 7: Instantaneous isosurface plots of the Q-criterion according to different operating orientations, coloured by velocity magnitude

5 Aerodynamic noise characteristics

5.1 Aerodynamic noise with respect to different crosswind velocity levels

Five vertical noise receivers are arranged 4 m from the geometric centre of the pantograph. The distance between two adjacent noise receivers satisfies a double relationship in which the coordinate relationship is listed in Tab. 2.

Table 2: Five vertical noise receivers on the leeward side (m)

Noise receivers	b1	b2	b3	b4	b5
x	1.22	1.22	1.22	1.22	1.22
y	-0.184	0.816	2.816	6.816	14.816
z	4	4	4	4	4

Fig. 8 shows the SPL distribution curves of the leeward side noise receiving points (b1-b5) under various crosswind velocities. As shown in Fig. 8, the SPLs increase significantly with increasing crosswind velocity. As the height above the ground increases, the SPL curves on the leeward side first decrease, then increase, and finally decrease again. When the ground height is 7.192 m (b4), the SPL reaches a maximum. The SPL distribution law does not change with changes in the crosswind velocity, and the direction of crosswind does not change the vertical SPL distribution characteristics.
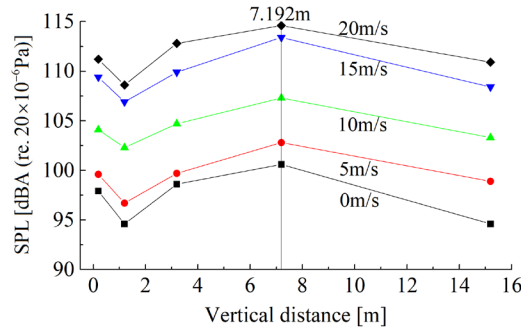

Figure 8: SPLs at vertical noise receiving points for several crosswind velocities

5.2 Acoustic attenuation

To investigate acoustic attenuation with respect to distance, six noise receiving points on the leeward side are breadthwise picked at 1, 2, 4, 8, 16 and 32 m from the vertical yz-plane at z=0. The length between each pair of nearby noise receiving points is double that between the previous pair.

Fig. 9 shows the acoustic attenuation characteristics with respect to transverse distance when the crosswind velocity is 15 m/s and illustrates the following features:
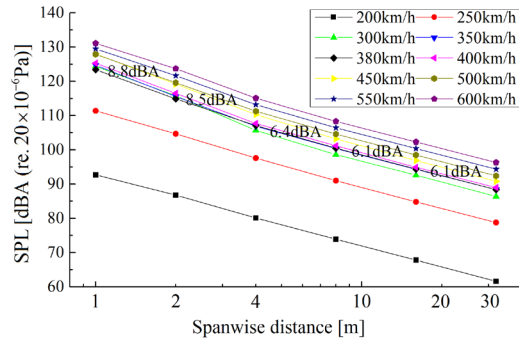
Figure 9: Acoustic attenuation with respect to transverse distance

5.2.1 Logarithmic distribution regularity

There is a linear relationship between the SPLs of the far-field aerodynamic noise and the logarithm of the transverse distance. When the pantograph operating speed is 350 km/h and the crosswind velocity is 15 m/s, the distribution regularity of SPL on the leeward side and the transverse distance (d) satisfy the logarithmic function:

$$L_{pm} = -22.34 \lg d + 122.78 \qquad d \geq 1\text{m} \tag{4}$$

There is a linear relationship between the SPLs of the far-field aerodynamic noise and the logarithm of the operating speed of the pantograph under crosswind. When the crosswind velocity is 15 m/s and the transverse distance is 32 m, the distribution regularity of SPL on the leeward side and the operating speed satisfy the logarithmic function:

$$L_{pm} = 60.49 \lg \frac{u}{u_0} + 69.94 \tag{5}$$

where u is the operating speed, and u_0=200 km/h. The slope in Eq. (5) is 60.49. Therefore, pantograph noises approximately grow as power law of operating speed to the order 6th under crosswind.

5.2.2 Acoustic attenuation characteristics

As the distance doubles, the magnitudes of acoustic attenuation have values of 8.8, 8.5, 6.4, 6.1, and 6.1 dBA on the leeward side. Specifically, the SPL magnitude of acoustic attenuation is about 6 dBA when the distance of the noise receiving point is far from 8 m. However, the SPL magnitude of acoustic attenuation is greater than 6 dBA when the noise receiving point is less than 8 m. This is probably because the noise receiving points at 1, 2 and 4 m distance are still not placed the acoustic and geometrical far-field of the pantograph. Adjacent noise receivers satisfying the double-fold relationship have attenuation amplitude of approximately 6 dBA on the spherical wave. On the cylindrical wave, the attenuation level of the SPL is approximately 3 dBA. These observations indicate that the acoustic attenuation characteristics of the pantograph under crosswind are analogous to the inflow transit a regular circular cylinder, which is a typical point source of radiated noise on a spherical wave [Yu, Li and Zhang (2013); Zhang, Zhang and Li (2017)].

5.3 Frequency spectral characteristics

5.3.1 Effects of different pantograph operating speeds

The spectrum of the aerodynamic noise generated by the full-scale pantograph at the b4 noise receiving point is displayed in Fig. 10. The aeroacoustic spectrum generated by the pantograph presents a very wide frequency range and is regarded as broadband noise, with the main energy-contained frequencies concentrated about between 400 and 1000 Hz. The main radiation energy comes from low-frequency noise, and mid-frequency noise is predominant compared to high-frequency aerodynamic noise. Moreover, the peak frequency of the pantograph is 512 Hz, and the corresponding SPL is approximately 106.4 dBA.
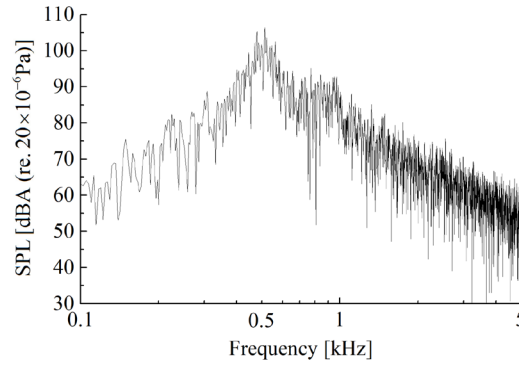

Figure 10: Noise spectrum from the pantograph at b4

The peak frequency distribution ranges of b4 are listed in Tab. 3. The distribution regularity of the peak frequency and pantograph operating speed satisfies the following functional relationship:

$$f_{A1} = 0.80u + 160.59 \tag{6}$$

$$f_{A2} = 0.82u + 176.85 \tag{7}$$

where f_{A1} and f_{A2} represent the lower limit and upper limit of the peak frequencies associated with pantograph operating speeds, respectively. As a result, the peak frequency of far-field aerodynamic noise is linearly related to the operating speed and is independent of the pantograph's operating orientation.

Table 3: The peak frequency range at b4 at different operating speeds

Operating speed (km/h)	Frequency (Hz)		Operating speed (km/h)	Frequency (Hz)	
	Lower limit	Upper limit		Lower limit	Upper limit
200	224	227	400	524	541
250	361	388	450	537	544
300	424	493	500	529	578
350	512	515	550	537	592
380	514	524	600	642	644

5.3.2 Effects of different crosswind velocities

Tab. 4 displays the peak frequency ranges at b4 when the pantograph is operated in the knuckle-downstream orientation model at 350 km/h. The crosswind velocities are 0, 5, 10, 15, and 20 m/s.

As the crosswind velocity increases, both the peak frequency and the amplitude of the spectral peak increase. The broadband noise at frequencies above the peak frequency also increases with increasing crosswind velocity, except at a crosswind velocity of 0 m/s. In addition, the aerodynamic noise frequency bandwidth range is always broader with crosswind than without crosswind. The linear fitting method is used to fit the peak frequency and crosswind velocity (v), and the following functional relationship is obtained:

$$f_{B1} = 13.12v + 282.99 \tag{8}$$

$$f_{B2} = 13.84v + 318.01 \tag{9}$$

where f_{B1} and f_{B2} are the lower limit and upper limit of the peak frequencies associated with the crosswind velocities.

Table 4: The peak frequency range at b4 at different crosswind velocities

Crosswind velocity (m/s)	First harmonic frequency (Hz)		Second harmonic frequency (Hz)		Third harmonic frequency (Hz)	
	Lower limit	Upper limit	Lower limit	Upper limit	Lower limit	Upper limit
0	287	329	586	613	905	916
5	335	368	666	689	—	1015
10	409	470	732	831	—	—
15	512	515	—	—	—	—
20	525	603	—	—	—	—

Therefore, the peak frequency of the far-field aerodynamic noise is linearly related to the crosswind velocity and is independent of the different pantograph operating orientations under crosswind. As the increase in the crosswind velocity corresponds to the increase in the yaw angle when the pantograph operating speed remain unchanged resulting to resultant velocity increase. As a result the vortex shedding frequency should not decrease with the increase of the yaw angle.

Tab. 4 also shows that there are three main frequencies in the absence of crosswind or when the crosswind velocity is very low. As the increase in the yaw angle, the main frequency is the first harmonic frequency, and the second harmonic and third harmonic frequencies disappear with increasing yaw angle increase. These frequencies disappear because the second harmonic frequency is associated with the fluctuating resistance and is mainly caused by the mutual effects of the wake of the panhead and the other components (e.g., balance arm, panhead support) [Zhang, Zhang and Li (2017)]. Therefore, as the yaw angle increases, the drag force decreases, but the side force increases. Thus, the second harmonic and third harmonic frequencies gradually disappear with increasing crosswind velocity.

5.3.3 Peak frequency-generating mechanism

Due to the complex geometric structure of the pantograph, which includes cylindrical bars, elliptical bars, cube bars and cuboid bars of various sizes and angles of inclination, the geometric characteristic length of the pantograph is difficult to determine. The characteristic frequency of the pantograph is studied using acoustic similarity regularity, and so the same geometric characteristic length can be applied in this paper. 100 mm is set as the geometric characteristic length of the pantograph, which corresponds to a yaw angle of 0° without crosswind, and the crosswind velocity is not considered. Fig. 11 displays the spectra of the aerodynamic noise from the pantograph at b4 at various pantograph operating speeds. *St* is solved using Eq. (10), which can be seen the blue dotted line tags in Fig. 11. This figure indicates that the aeroacoustic spectra radiated by the pantograph demonstrate a certain acoustic similarity for the same *St*. Additionally, the shedding frequency based on the geometric characteristic length of *l*=100 mm is *St*=0.318, with two other minor frequencies at *St*=0.628 and *St*=0.941.

The flow past a circular cylinder corresponding to the Strouhal Number (*St*) satisfied Eq. (10).

$$St = \frac{f_0 \times l}{u} \tag{10}$$

where f_0 is the vortex shedding frequency, l is the geometric characteristic length and u is the inflow velocity.
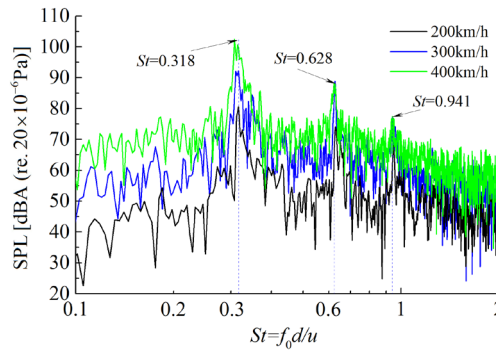

Figure 11: Spectra of noise from the pantograph at different operating speeds

Fig. 12 reveals the spectra of the aerodynamic noise of the contact strip and balance arm at b4 noise receiving point at various operating speeds without crosswind. These spectra exhibit three distinct peaks. The *St* of the first peak are almost the same at the various operating speeds and are similar to the vortex shedding frequency of the cylindrical bar, which implies that the aerodynamic noise of the contact strip and balance arm indicate a certain degree of acoustic similarity at the same *St*. The comparative analysis of Fig. 11 and Fig. 12 shows that the aeolian tone characteristics of the contact strip and balance arm generate peak noise, and the dominant peak frequency is related to the vortex shedding frequency.
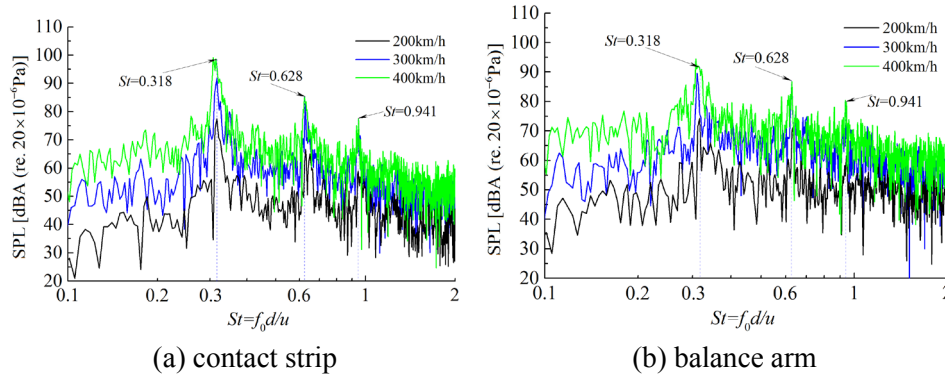
Figure 12: Spectra of noise from the key components at different operating speeds

According to Eq. (10), Fig. 11 uses 100 mm as the geometric characteristic length. By using the same *St*=0.318 in Fig. 12, it is easy to obtain the following result:

$$l_L = \frac{St_L \times l}{St} = \frac{0.2 \times 100 \text{ mm}}{0.318} \approx 62.89 \text{ mm} \tag{11}$$

The result from Eq. (11) is close to the diameter (60 mm) of the balance arm and the width (60 mm) of the contact strip. Furthermore, the results indicate that the vortex shedding generated by the panhead (balance arm and contact strip) produces tonal noise, with the dominant peak frequency corresponding to the vortex shedding frequency, because the axis of the contact strip and balance arm are the most perpendicular to the inflow orientation and are located outside the wake region of any other components of the pantograph.

6 Conclusions

In this paper, we used the LES and FW-H methods together to perform a numerical study on the aerodynamic and aeroacoustic behaviours of the flow past the DSA380 pantograph under crosswind. The following conclusions were drawn.

(1) Asymmetric characteristics of the flow field are observed using instantaneous vortexes and Q-criterion under crosswind. Additionally, the flow field distribution and the near-field aerodynamic performance of the knuckle-downstream orientation model are superior to those of the knuckle-upstream orientation model. Vortex shedding, flow separation and recombination around the pantograph are the key factors for aerodynamic noise generation.

(2) The aerodynamic noise radiated by the pantograph is approximately 6 dBA when the spanwise distance of the noise receiving point is farther than 8 m, in which the far-field noise conditions are satisfied. This result indicates that the attenuation characteristics of the far-field aerodynamic noise of the pantograph are similar with respect to the flow past a regular circular cylinder under crosswind, which is a typical point source radiation on a spherical wave.

(3) The analysis of the frequency spectral characteristics shows that the frequency band is wider with crosswind than without crosswind. The peak frequency exhibits a linear relationship with the operating speed, and a linear relationship is also suitable for the

peak frequency and crosswind velocity. The dominant peak frequency generated by the contact strip and the balance arm is related to the vortex shedding frequency. However, the influence of the coupling between train running speed and crosswind velocity on the pantograph spectrum needs further study.

Conflicts of Interest: The authors declare that they have no conflicts of interest to report regarding the present study.

References

Baker, C. (2010): The flow around high speed trains. *Journal of Wind Engineering and Industrial Aerodynamics*, vol. 98, pp. 277-298.

Curle, N. (1955): The influence of solid boundaries upon aerodynamic sound. *Proceedings of the Royal Society of London, Series A, Mathematical and Physical Sciences*, vol. 231, no. 1187, pp. 505-514.

Ffowcs-Williams, J. E.; Hawkings, D. L. (1969): Sound generation by turbulence and surfaces in arbitrary motion. *Philosophical Transactions for the Royal Society of London, Series A, Mathematical and Physical Sciences*, vol. 264, no. 1151, pp. 321-342.

Flynn, D.; Hemida, H.; Baker, C. (2016): On the effect of crosswinds on the slipstream of a freight train and associated effects. *Journal of Wind Engineering and Industrial Aerodynamics*, vol. 156, pp. 14-28.

Ikeda, M.; Suzuki, M.; Yoshida, K. (2006): Study on optimization of panhead shape possessing low noise and stable aerodynamic characteristics. *Quarterly Report of RTRI*, vol. 47, no. 2, pp. 72-77.

Latorre Iglesias, E.; Thompson, D. J.; Smith, M. G. (2017): Component-based model to predict aerodynamic noise from high-speed train pantographs. *Journal of Sound and Vibration*, vol. 394, pp. 280-305.

Li, T.; Qin, D.; Zhang, J. (2019): Effect of RANS turbulence model on aerodynamic behavior of trains in crosswind. *Chinese Journal of Mechanical Engineering*, vol. 32, pp. 1-12.

Lighthill, M. J. (1952): On sound generated aerodynamically. I. General theory. *Proceedings of the Royal Society of London, Series A, Mathematical and Physical Sciences*, vol. 211, no. 1107, pp. 564-587.

Liu, X. W.; Hu, Z. W.; Thompson, D. J.; Jurdic, V. (2018): Reduction of aerodynamic noise from square bars by introducing spanwise waviness. *Journal of Sound and Vibration*, vol. 435, pp. 280-305, 323-349.

Mellet, C.; Létourneaux, F.; Poisson, F.; Talotte, C. (2006): High speed train noise

emission: latest investigation of the aerodynamic/rolling noise contribution. *Journal of Sound and Vibration*, vol. 293, no. 3, pp. 535-546.

Nagakura, K. (2006): Localization of aerodynamic noise sources of Shinkansen trains. *Journal of Sound and Vibration*, vol. 293, no. 3, pp. 547-556.

Sagaut, P. (2006): *Large Eddy Simulation for Incompressible Flows: An Introduction*. Springer, Berlin.

Sueki, T.; Ikeda, M.; Takaishi, T. (2009) Aerodynamic noise reduction using porous materials and their application to high-speed pantographs. *Quarterly Report of RTRI*, vol. 50, no. 1, pp. 26-31.

Tan, X. M.; Yang, Z. G.; Tan, X. M.; Wu, X. L.; Zhang, J. (2018): Vortex structures and aeroacoustic performance of the flow field of the pantograph. *Journal of Sound and Vibration*, vol. 432, pp. 17-32.

Thompson, D. J.; Latorre Iglesias, E.; Liu, X.; Zhu, J.; Hu, Z. (2015): Recent developments in the prediction and control of aerodynamic noise from high-speed trains. *International Journal of Rail Transportation*, vol. 3, no. 3, pp. 119-150.

Yu, H. H.; Li, J. C.; Zhang, H. Q. (2013): On aerodynamic noises radiated by the pantograph system of high-speed trains. *Acta Mechanica Sinica*, vol. 29, no. 3, pp. 399-410.

Zhang, J.; Xiao, X.; Wang, D.; Yang, Y.; Fan, J. (2018): Source contribution analysis for exterior noise of a high-speed train: experiments and simulations. *Shock and Vibration*, vol. 2018, pp. 1-13.

Zhang, Y. D.; Zhang, J. Y.; Li, T. (2016): Research on aerodynamic noise source characterization and noise reduction of high-speed trains vehicle. *Journal of the China Railway Society*, vol. 38, no. 7, pp. 40-49.

Zhang, Y. D.; Zhang, J. Y.; Li, T.; Zhang, L. (2017): Investigation of the aeroacoustic behavior and aerodynamic noise of a high-speed train pantograph. *Science China Technological Sciences*, vol. 60, no. 4, pp. 561-575.

Zhang, Y. D.; Zhang, J. Y.; Li, T.; Zhang, L.; Zhang, W. H. (2016): Research on aerodynamic noise reduction for high-speed trains. *Shock and Vibration*, vol. 2016, pp. 1-21.

Zhang, Y. D.; Zhang, J. Y.; Zhang, W. H. (2017): Analysis of aerodynamic noise characteristic of high-speed pantograph. *Journal of the China Railway Society*, vol. 39, no. 5, pp. 47-56.